Journal of Hydraulic Research

ISSN: 0022-1686 (Print) 1814-2079 (Online) Journal homepage: http://iahr.tandfonline.com.tandf-prod.literatumonline.com/loi/tjhr20

Steady-flow experiments in urban areas and anisotropic porosity model

Mirjana Velickovic, Yves Zech & Sandra Soares-Frazão

Journal of Hydraulic Research, 2016
http://dx.doi.org/10.1080/00221686.2016.1238013

Research paper

Steady-flow experiments in urban areas and anisotropic porosity model

MIRJANA VELICKOVIC, PhD Student, *Institute of Mechanics, Materials, and Civil Engineering, Université catholique de Louvain, Louvain-la-Neuve, Belgium*; *Fonds pour la Formation à la Recherche dans l'Industrie et dans l'Agriculture, Brussels, Belgium*
Email: mirjana.velickovic@uclouvain.be

YVES ZECH (IAHR Member), Emeritus Professor, *Institute of Mechanics, Materials, and Civil Engineering, Université catholique de Louvain, Louvain-la-Neuve, Belgium*
Email: yves.zech@uclouvain.be

SANDRA SOARES-FRAZÃO (IAHR Member), Professor, *Institute of Mechanics, Materials, and Civil Engineering, Université catholique de Louvain, Louvain-la-Neuve, Belgium*
Email: sandra.soares-frazao@uclouvain.be (author for correspondence)

ABSTRACT
Modelling flow through an urban area is challenging because of the significant difference between the scale of individual streets and the whole district scale. This paper presents idealized experiments where buildings are represented by square blocks. The experiments were designed to highlight the effect of the street width and orientation to the main flow direction. In addition, a porosity model is developed for representing the urban district as a whole without considering the detailed geometry of the streets, but accounting for the main effects on the flow. The model introduces a tensor of drag coefficients aimed at representing directional effects. The drag coefficients are calibrated and validated using the experimental results.

Keywords: Drag coefficient; laboratory experiment; porosity model; shallow-water; two-dimensional model; urban flood modelling

1 Introduction

The ability of modelling floods accurately is important for various purposes, such as the assessment of flood-induced risks, effects of flood mitigation measures or the design of emergency plans (e.g. Paquier, Tachrift, Riviere, & El Kadi, 2009). Simulating a flood event through areas partially occupied by urban infrastructures is challenging due to the scale difference between the urban streets (~ 10 m) and the space outside the city (~ 100 m).

If a high level of accuracy is required, the buildings are often represented as a fictitious conventional raise of the bottom level or as "holes" in the two-dimensional mesh surrounded by wall boundary conditions. A finer mesh is then used in the streets and especially in the crossroads to reproduce the flow with sufficient details. The streets often offer a low resistance to the flow and behave as channels with relative smooth boundaries (concrete or asphalt) compared to rural areas. In this kind of detailed model, the direction of flow propagation is properly accounted for (e.g. Gallegos, Schubert, & Sanders, 2009). In regards the required mesh refinement over the street width Schubert, Sanders, Smith, and Wright (2008) suggest that a mesh should span streets by approximately three cells over the street width to achieve a good balance between accuracy and computational effort. In a study based on detailed experimental measurements, Soares-Frazão and Zech (2008) considered that a good accuracy in the representation of two-dimensional features, especially at the crossroads, was achieved with 10 computational cells over the street width. Of course, such mesh refinements result in a significant computational cost and require detailed topographic data to be used. In order to decrease the computational cost, different approaches have been proposed that belong to two main families: sub-grid models and continuum models.

In the sub-grid models, the element size is of the order of the street width or even larger, implying that an element could be partially occupied by a building. Macroscopic parameters, such

Received 30 June 2015; accepted 14 September 2016/Currently open for discussion.

ISSN 0022-1686 print/ISSN 1814-2079 online
http://www.tandfonline.com

as the porosity, are then assigned to each mesh element to reproduce their inner complex geometry. For instance, McMillan and Brasington (2007) assigned a "porosity" parameter to each element to account for the reduction of water storage capacity and the reduced flow conveyance due to the presence of buildings in a given element. In this approach, the porosity assigned to each element is the ratio between the actual area of the element available for the flow (i.e. without buildings) and the total area of the element. They reported that this approach enabled reduction of the model run-time by an order of magnitude and was a viable method providing a realistic representation of general flood evolution. However, Mason, Horritt, Hunter, and Bates (2007) compared the sub-grid porosity model with high resolution simulation for the 2005 flood event in Carlisle, UK, and concluded that this model was inadequate for replicating real urban hydraulics. Sanders, Schubert, and Gallegos (2008) improved the sub-grid porosity model by adding two distinct conveyance porosities to capture the anisotropy of the medium, and modelled the resistance exerted by the buildings to the flow by a drag coefficient. However, they observed that the results were dependent on the shape of the mesh and the elements size. Liang, Falconer, and Lin (2007) developed a coupled surface and subsurface flow models. Among others, they modelled floods in urban media by representing each building individually as a raise of porous bottom, even including the possibility of some flow throughout the building.

Another way to consider the problem is to use a continuum approach. The simplest one involves increasing Manning's friction coefficient in the urban area to account for its increased flow resistance. However, the main drawbacks of this approach is the inaccurate representation of the total volume of flowing water and the calibration of the Manning coefficient in the urban area, leading to unphysical values. Continuum approaches are also defined in Bachmat and Bear (1986), and are widely used in the field of flow modelling in porous media. The approach involves substituting a fictitious homogeneous medium for the heterogeneous medium constituted by the fluid and the solid matrix. In the homogeneous medium, adapted averaging rules should be defined to account for the small-scale complex geometry. The variables have to be globally representative of the pore-scale variables. The bulk properties are called the macroscopic (or global) properties and the pore scale properties are referred to as the microscopic (or local) ones. Following these ideas, an urban medium can be assimilated to a large two-dimensional continuous porous medium (Fig. 1) in which the porosity is continuous all over the urban medium, and the variables of interest are the macroscopic (district scale) water depth and velocity. The main practical difference with sub-grid models is that the same porosity value is assigned to all the computational elements of the urban medium, no matter how much space is really occupied by a building in each element. Such approaches have the key advantage of being mesh-independent.

Various forms of the governing equations of the porosity model have been successively developed by Defina, D'Alpaos, and Mattichio (1994), Defina (2000), Bates (2000), Lhomme (2006), Guinot and Soares-Frazão (2006), Soares-Frazão, Lhomme, Guinot, and Zech (2008), Velickovic, Van Emelen, Zech, and Soares-Frazão (2010), Velickovic, Zech, and

Figure 1 Similarity of an urban area to a porous medium (New York, USA, image: Google Earth, Landsat, 1995)

Soares-Frazão (2012) and Velickovic (2012). The porosity is commonly defined as the ratio between the area available for the flow (i.e. the streets) and the total area of the urban zone in the computational domain. It is independent of the water depth as the building walls are considered to be vertical and infinitely high, so that they cannot be submerged. The resistance opposed by the buildings is usually modelled by a closure relation of the type of a drag force. Other definitions of the porosity could be considered, for example conveyance porosity instead of storage porosity; see among others Guinot (2012) and Kim, Sanders, Famiglietti, and Guinot (2015).

The porosity equations are often solved by the finite volume method (e.g. Cea & Vázquez-Cendón, 2010; Finaud-Guyot, Delenne, Lhomme, Guinot, & Llovel, 2010; Guinot & Soares-Frazão, 2006). Guinot and Soares-Frazão (2006) developed a modified HLL (Harten–Lax–Van Leer) Riemann solver on unstructured grids and treated the source terms arising from the bottom slope and the porosity gradient by an upwind approach. Cea and Vázquez-Cendón (2010) presented and compared two different Roe-like numerical discretizations of the porosity equations, both of them being high-order schemes. Finaud-Guyot et al. (2010) developed an approximate-state solver based on the assumption that both waves of the Riemann problem are rarefaction waves, and used it in porosity-based simulations. In all these models, the key issue lies in the source terms accounting for the drag effect of the buildings on the flow, and the way to account for preferential flow directions in the urban area, for example large streets. Recently, Guinot (2012) developed a multiple porosity model assuming that the urban medium is the superimposition of various porous media with different characteristics. He considered the resistance to the flow to be due to an exchange of momentum between the overlapping media.

The model discussed in the present study is of the "single porosity model" type, or simply "porosity model": a single value of the porosity parameter, defined by ϕ, is considered, and preferential flow directions are taken into account through directional drag effects. In order to validate porosity models, laboratory experiments are generally used, consisting in placing square blocks representing buildings in a flume. Among the existing datasets, four main types can be considered: (i) experiments conducted in a straight flume with a rectangular cross-section in which dam break flow or steady flows are simulated (e.g. Soares-Frazão & Zech, 2008); (ii) experiments conducted in model cities, where the main focus is set on the streets themselves (Araud et al., 2012; Ishigaki, Keiichi, & Kazuya, 2003; Ishigaki, Nakagawa, & Baba, 2004); (iii) experiments in scale models of real valleys, e.g. the Toce valley (Italy), in which a transient discharge is imposed at the upstream section of the model (Testa, Zuccalà, Alcrudo, Mulet, & Soares-Frazão, 2007), and (iv) field cases as presented, e.g. by Bazin (2013). In the laboratory cases, the "buildings" are arranged so that they form a periodic pattern, either staggered or aligned, the street direction being either aligned or forming an angle with the main flow direction.

In this paper, we present new experiments conducted in the Hydraulics Laboratory of the Université catholique de Louvain (UCL), Belgium, aimed at studying anisotropic effects on the flow. These new experiments consist in varying the street width and city orientation under steady flow conditions. Then, the proposed porosity model is briefly explained and a new expression is proposed for the bulk resistance exerted by the buildings on the flow, this expression accounting for anisotropic effects. Finally, the results obtained using the proposed model are compared to experiments and conclusions are drawn about the modelling of anisotropic and directional effects.

2 Experiments

The laboratory experiments were conducted in the Hydraulics Laboratory of the Institute for Mechanical, Materials and Civil Engineering of the UCL, Belgium. The test channel has a horizontal bed, is 36 m long with a usable length of about 30 m, and 3.6 m wide (Fig. 2).

Various building layouts were tested: the buildings were either aligned with each other (e.g. Lhomme, 2006), or staggered (Lhomme, Soares-Frazão, Guinot, & Zech, 2007), and the city streets were either aligned with the flume axis or rotated by an angle of 22.5° (e.g. Soares-Frazão, Spinewine, Duthoit, Deswijsen, & Zech, 2006; Soares-Frazão & Zech, 2008) as illustrated in Fig. 3.

As the flume was initially designed to simulate dam-break flows, the gate was opened suddenly to simulate the dam-break. For steady-flow experiments, the upstream gate always remained open so that it did not control the flow, and the discharge was imposed via a regulation system; the pump rotation speed being adjusted according to the actual discharge measured by a flowmeter, with an accuracy of about $1\,\mathrm{l\,s^{-1}}$. Arrays of 5 × 5 square wooden blocks representing buildings were arranged in the flume as illustrated in Fig. 3. The blocks formed a network of perpendicular streets with different widths and different orientations. Additional blocks were placed beside the

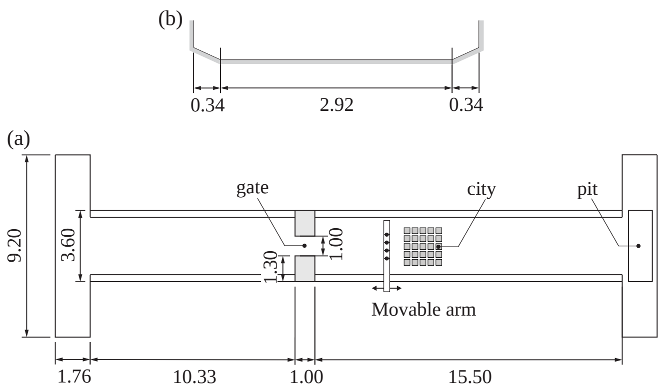

Figure 2 Experimental set-up and flume dimensions (m): (a) plane view and (b) cross-section

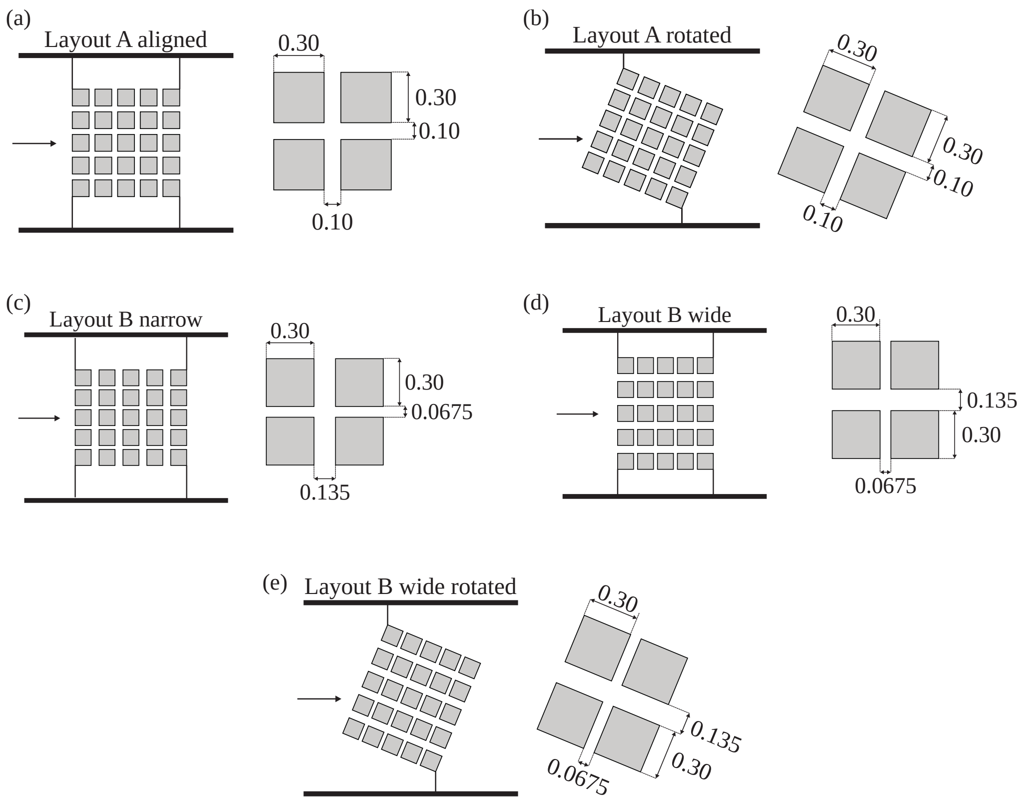

Figure 3 Plane view of the tested layouts in steady flow (dimensions are in metres): (a) aligned layout A; (b) rotated layout A; (c) layout B with the narrow streets aligned with the main direction of the flume; (d) layout B with the wide streets aligned with the main direction of the flume; and (e) rotated layout B

city to prevent the flow from by-passing it. This had the advantage of increasing the head losses and thus the difference of water level between upstream and downstream of the city, and so making the effect of the city more visible.

All layouts of Fig. 3 presented the same porosity, i.e. the ratio between the area available for the flow (i.e. the streets) and the total area of the urban zone in the computational domain, with a value $\phi = 0.4375$. The layouts of Fig. 3a, 3c and 3d are called "aligned" because their main axes are aligned to axes x and y. In contrast, layouts of Fig. 3b and 3e are called "rotated." Layouts of Fig. 3a and 3b are designated by the letter "A" because all the streets have the same widths, and layouts of Fig. 3c, 3d and 3e are designated by the letter "B." The base of the buildings has dimensions of 0.3 m × 0.3 m, the streets in layout A are 0.1 m wide, and in layout B, the streets widths are 0.135 m and 0.0675 m, respectively.

In all experiments, the downstream water level is a free outflow into a pit. The tested flow discharges are summarized in Table 1. In all cases, the Manning friction coefficient for the channel bed is 0.01, according to previous works carried out on this flume (e.g. Soares-Frazão & Zech, 2008).

The water level is measured by four ultrasonic probes (accuracy of about 0.1 mm) fixed to a movable arm that can sweep the flume length so that water levels along four axes (Fig. 4) are measured at once. The measuring axes are located at the centre of the streets to prevent any perturbation effect from the building walls.

Table 1 Tested discharges for the layouts of Fig. 3 (steady flow)

Layout	Figure	Q (l s^{-1})
A aligned	3a	43
		58
		63
		75
		86
		103
A rotated	3b	75
		100
B aligned narrow	3c	25
		35
		41
		50
B aligned wide	3d	52
		64
		75
		80
		92
		99
B rotated	3e	75
		100

Figure 5 shows the water profiles measured by the four probes in layout A for a discharge $Q = 75\,\mathrm{l\,s^{-1}}$. It can be seen that the water surface upstream of the city is almost horizontal and then drops suddenly at the entrance of the city at $x = 5$ m.

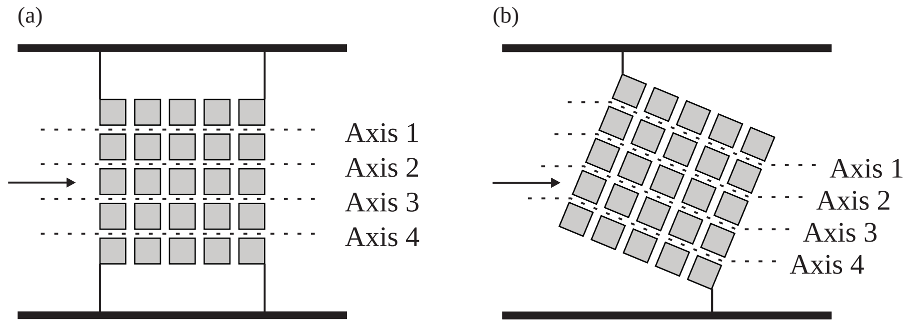

Figure 4 Axes of measurement of the four water profiles for (a) the aligned layouts; and (b) the rotated layout. Axes are labelled from 1 to 4

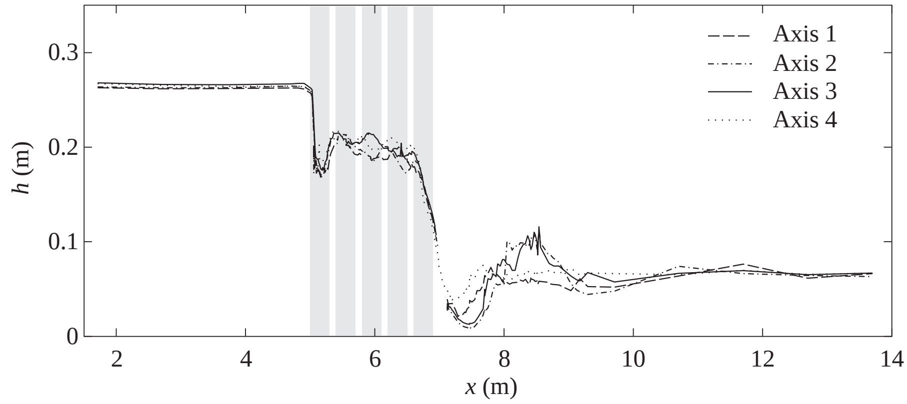

Figure 5 Water profiles measured by the four probes for the aligned layout A for a discharge $Q = 75\,\mathrm{l\,s^{-1}}$ (see the location of axes in Fig. 4a). The grey rectangles represent the buildings

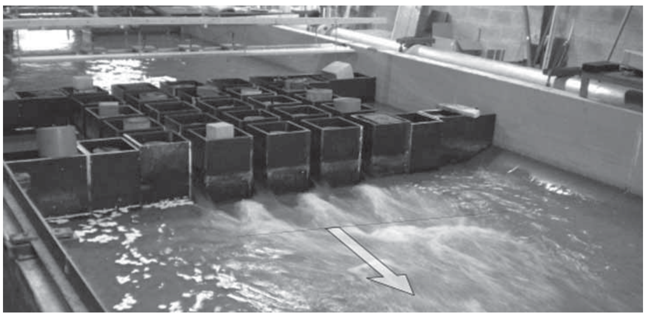

Figure 6 Photograph of the flow downstream of the model city (layout A, $Q = 75\,\mathrm{l\,s^{-1}}$)

In the urban area between $x = 5.3$ m and $x = 6.6$ m, the water level has a slight tendency to decrease. At the exit of the city, the water level drops again below the critical depth (0.04 m) to form a supercritical flow, followed by a hydraulic jump (at $x = 7.7$ m for axes 1 and 4 and $x = 8.5$ m for axes 2 and 3, see also the photograph in Fig. 6), itself followed by some perturbations until $x = 10.5$ m, after which the water profile remains almost horizontal again until the downstream section of the flume.

Figure 7 illustrates the results for the aligned layout A for discharges from $43\,\mathrm{l\,s^{-1}}$ to $103\,\mathrm{l\,s^{-1}}$. For sake of clarity, the

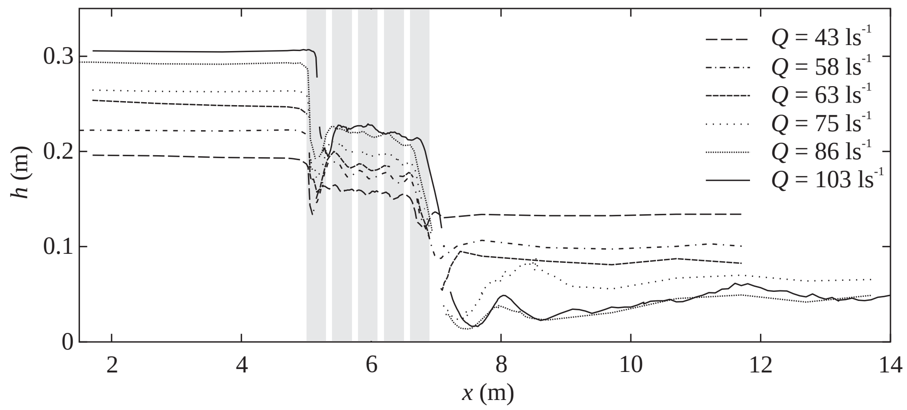

Figure 7 Water profile for the aligned layout A for all tested discharges (the four profiles are averaged for each discharge). The grey rectangles represent the buildings

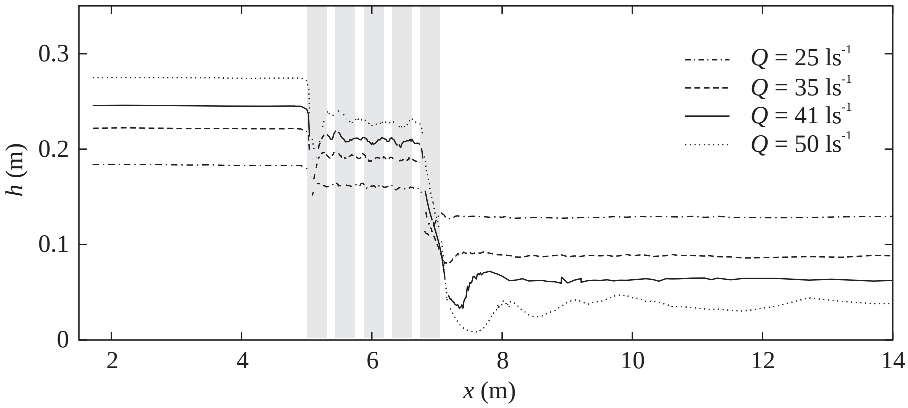

Figure 8 Water profile for the aligned layout "B narrow" along the narrow streets in the main flow direction, for all the tested discharges (the four profiles are averaged for each discharge). The grey rectangles represent the buildings

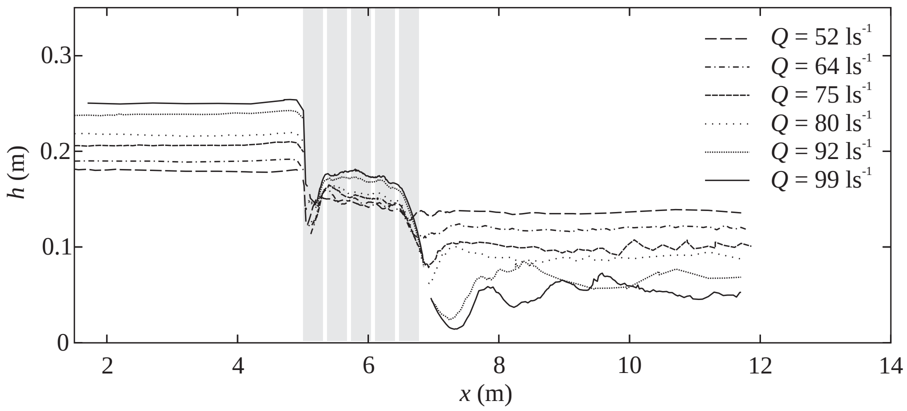

Figure 9 Water profile for the aligned layout "B wide" along the wide streets in the main flow direction, for all the tested discharges (the four profiles are averaged for each discharge). The grey rectangles represent the buildings

water profiles are averaged on the four parallel streets so that there is only one curve per discharge. Unsurprisingly, the difference between water levels upstream and downstream of the city increases with the discharge.

Figure 8 shows the results for layout "B narrow" along the narrow streets in the main flow direction. The discharges range from $25\,\mathrm{l\,s^{-1}}$ to $50\,\mathrm{l\,s^{-1}}$. By comparison with layout A (Fig. 7), in which the streets are wider (0.1 m wide while only 0.0675 m wide in layout B), we can expect the difference between water levels upstream and downstream of the city to be larger for the same discharge. Indeed, comparing the water profile for $Q = 43\,\mathrm{l\,s^{-1}}$ in Fig. 7 and the water profile for $Q = 41\,\mathrm{l\,s^{-1}}$ in Fig. 8, shows that this difference has increased.

Figure 9 shows the results for layout "B wide" along the wide streets in the main flow direction. The discharges range from $52\,\mathrm{l\,s^{-1}}$ to $99\,\mathrm{l\,s^{-1}}$. The wide streets are wider (0.135 m) than the streets of layout A (0.10 m) and the narrow ones of layout "B narrow" are narrower (0.0675 m) than in layout A (0.10 m). By comparison with these two layouts (Figs 7 and 8), similar discharge presents lower differences between upstream and downstream water levels.

The rotated layouts A and B are tested with a discharge of $75\,\mathrm{l\,s^{-1}}$ and $100\,\mathrm{l\,s^{-1}}$. The water profiles for layout A are shown in Fig. 10 and the ones for layout B, in Fig. 11. For layout A, the water level upstream of the city is lower than in the aligned case for the same discharges (Fig. 7). This could be explained by the fact that the difference of water level ahead and behind the city is proportional to the resistance that the city offers to the flow: the higher the resistance, the higher the difference of water level. The aligned cases offer four inlets to the flow, while the rotated cases offer eight inlets, so a better conveyance although the flow is more deviated to enter the streets. For layout B (Fig. 11), due to the fact that four streets are wider, the gain of conveyance is less evident and the head loss is comparable to the aligned wide case (Fig. 9).

3 Porosity model

3.1 *Governing equations*

The porosity ϕ is defined as the ratio between the plane-view area available for the flow (in practice, the streets) and the whole urban district area. In practice this porosity indicates the relative room available for water storage in a control volume. The 2D shallow water equations with porosity can be written in the

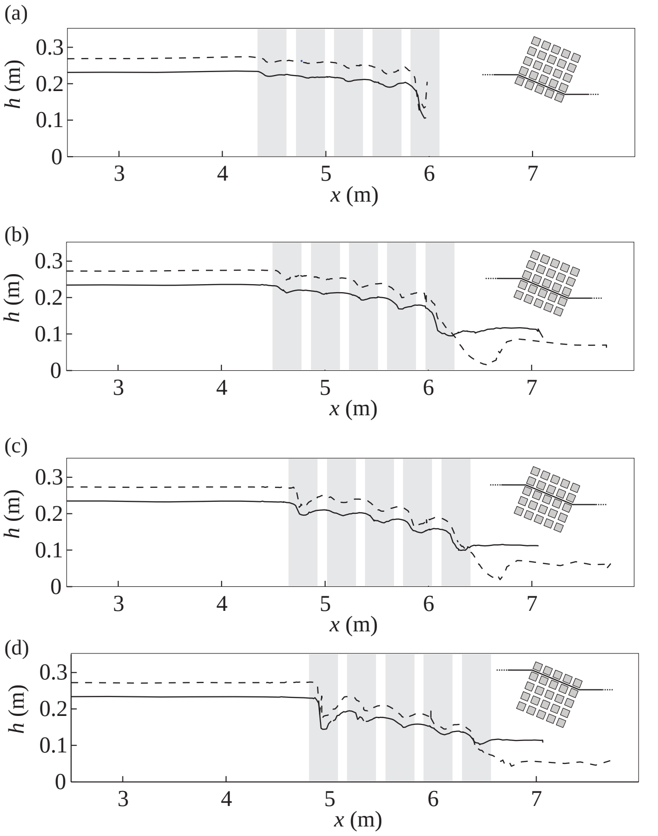

Figure 10 Water profiles for the rotated layout A, for $Q = 75\,\mathrm{l\,s^{-1}}$ (continuous line) and $Q = 100\,\mathrm{l\,s^{-1}}$ (dashed line), along (a) axis 1, (b) axis 2, (c) axis 3 and (d) axis 4. The grey rectangles represent the buildings

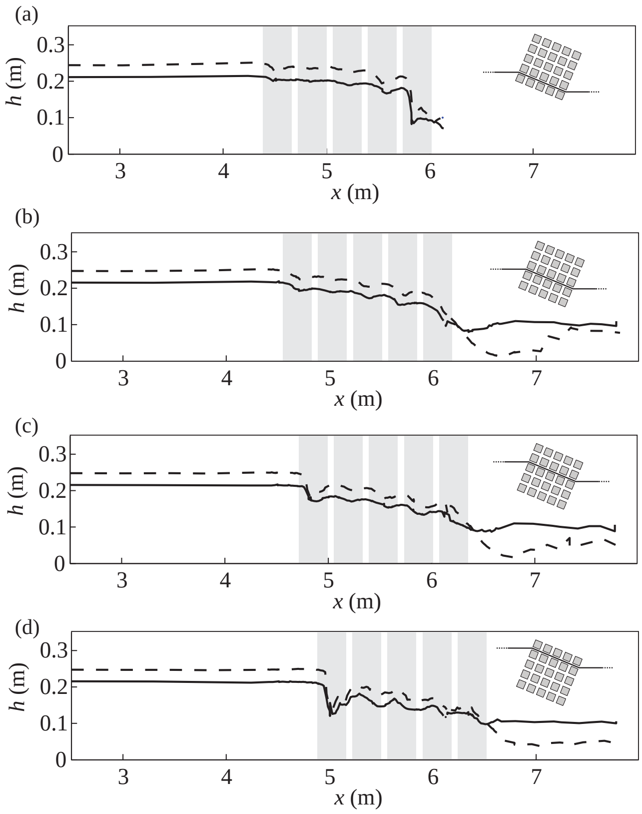

Figure 11 Water profiles for the rotated layout B, for $Q = 75\,\mathrm{l\,s^{-1}}$ (continuous line) and $Q = 100\,\mathrm{l\,s^{-1}}$ (dashed line), along (a) axis 1, (b) axis 2, (c) axis 3 and (d) axis 4 (see Fig. 4 for the name of axes). The grey rectangles represent the buildings

conservation form as (Soares-Frazão et al., 2008):

$$\frac{\partial \mathbf{U}}{\partial t} + \frac{\partial \mathbf{F}}{\partial x} + \frac{\partial \mathbf{G}}{\partial y} = \mathbf{S} \tag{1}$$

where

$$\mathbf{U} = \begin{pmatrix} \phi\, h \\ \phi\, uh \\ \phi\, vh \end{pmatrix}, \quad \mathbf{F} = \begin{pmatrix} \phi\, uh \\ \phi\, u^2h + \phi\dfrac{gh^2}{2} \\ \phi\, uvh \end{pmatrix},$$

$$\mathbf{G} = \begin{pmatrix} \phi\, vh \\ \phi\, uvh \\ \phi\, v^2h + \phi\dfrac{gh^2}{2} \end{pmatrix} \tag{2}$$

$$\text{and } \mathbf{S} = \begin{pmatrix} 0 \\ \phi\, gh\,(S_{0x} - S_{fx} - S_{lx}) + \dfrac{gh^2}{2}\dfrac{\partial \phi}{\partial x} \\ \phi\, gh\,(S_{0y} - S_{fy} - S_{ly}) + \dfrac{gh^2}{2}\dfrac{\partial \phi}{\partial y} \end{pmatrix}$$

where ϕ is the porosity, h is the water depth, u and v are the components of the depth-averaged velocity vector $\mathbf{V}$ in x- and y-directions, S_{0x} and S_{0y} are the bed slope components, S_{fx} and S_{fy} are the part of the flow resistance due to bed friction and S_{lx} and S_{ly} are the part of the flow resistance due to drag forces exerted by the buildings on the flow. So, a drag coefficient has to be defined and calibrated, taking into account, as far as possible, the anisotropic character of the urban medium.

In this study, we focus on periodic media like the one illustrated in Fig. 12, where the buildings have a rectangular footprint and are aligned with each other, forming a network of perpendicular streets, like in the experiments presented in Section 2. A local reference system (ξ, η) is defined, aligned

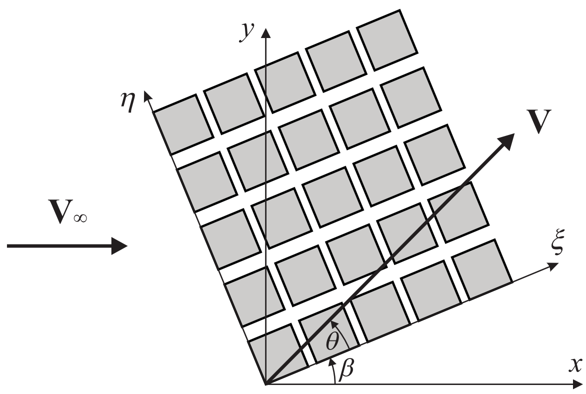

Figure 12 Footprints of buildings in a periodic medium constituted by aligned rectangle-based buildings, and definition of the angle θ. In this example, the x-direction is aligned with the main flow direction

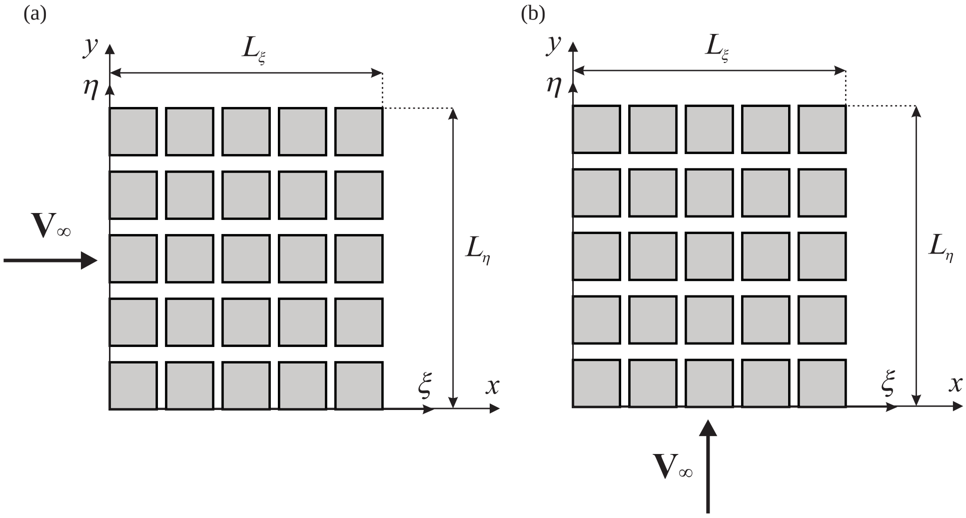

Figure 13 Reference situations: (a) main flow parallel to the ξ-direction; (b) main flow in the η-direction

with the street directions (in Fig. 12 ξ is aligned with the widest streets) making an angle β with the (x, y) directions. The flow is of course deviated from the main flow direction by the non-alignment of the streets but, also, the bulk velocity might not be aligned with the streets. So we can assume that the bulk velocity $\mathbf{V}$ presents an angle θ to the ξ direction. If the street widths are the same in ξ- and η-directions the layout is isotopic, while anisotropic if the widths are distinct.

It is assumed that the drag resistance S_l depends on the street width and orientation. If we consider a street arrangement with the street direction ξ parallel to the main flow direction x (Fig. 13a), it can be assumed that the bulk velocity is also generally parallel to this x-direction: indeed, there is no reason that the main flow be significantly deviated (the perpendicular streets do not induce asymmetrical effects) and the angle θ may be assumed as zero. So, with this assumption, the drag force only exerts in the same x-direction, in such a way that we can define a drag coefficient C_ξ:

$$\mathbf{S}_l = \begin{pmatrix} S_{lx} \\ S_{ly} \end{pmatrix} = \begin{pmatrix} S_{l\xi} \\ 0 \end{pmatrix} = \begin{pmatrix} \dfrac{1}{L_\xi} C_\xi \dfrac{u^2}{2g} \\ 0 \end{pmatrix} = \begin{pmatrix} C'_\xi \dfrac{u^2}{2g} \\ 0 \end{pmatrix} \tag{3}$$

The source terms of gravity and of friction in Eq. (2) are distributed along the whole length of the city, while a drag force in generally located at one point in front of the obstacle to the flow. So, for consistency, this local force is fictitiously distributed along the flow path by dividing the force by the length of this path, following the approach also presented by Sanders et al. (2008) and Kim et al. (2015), where the drag coefficient C_D is multiplied by parameters representing the frontal area of the obstruction by unit planform area. Here, we propose to replace the drag coefficient C_ξ by C'_ξ, which becomes the (dimensional) parameter to calibrate.

The drag coefficients C_η that would prevail in case of main flow in the η direction, with the same assumption of not deviated bulk velocity (Fig. 13b), is distinct from C_ξ if the street widths are distinct:

$$\mathbf{S}_l = \begin{pmatrix} S_{lx} \\ S_{ly} \end{pmatrix} = \begin{pmatrix} 0 \\ S_{l\eta} \end{pmatrix} = \begin{pmatrix} 0 \\ \dfrac{1}{L_\eta} C_\eta \dfrac{v^2}{2g} \end{pmatrix} = \begin{pmatrix} 0 \\ C'_\eta \dfrac{v^2}{2g} \end{pmatrix} \tag{4}$$

In the example of Fig. 12, the drag coefficient C_ξ is smaller than C_η, representing the fact that the flow offers less resistance in a direction where the streets are wider than in the normal direction where the streets are narrower.

If we now consider a bulk velocity deviated from the main flow direction, we can assume that each component of this velocity exerts a different drag force:

$$\mathbf{S}_l = \begin{pmatrix} S_{lx} \\ S_{ly} \end{pmatrix} = \begin{pmatrix} C'_\xi \dfrac{||\mathbf{V}||\, u}{2g} \\ C'_\eta \dfrac{||\mathbf{V}||\, v}{2g} \end{pmatrix} = \frac{||\mathbf{V}||}{2g} \begin{pmatrix} C'_\xi & 0 \\ 0 & C'_\eta \end{pmatrix} \begin{pmatrix} u \\ v \end{pmatrix}$$

$$= \frac{||\mathbf{V}||}{2g} \left(\mathbf{C}_{D,\,\xi\eta} \cdot \mathbf{V}\right) \tag{5}$$

This formulation suggests modelling the drag with a tensor $\mathbf{C}_D$ and not just by a scalar. An interesting property is the following: if the system of street co-ordinates (ξ, η) is aligned with the main flow direction x, the non-diagonal components of $\mathbf{C}_D$ are equal to zero (Bear, 1972), even if the medium is anisotropic. This property will be used in this study to calibrate $\mathbf{C}_D$.

If the streets are not aligned with the main flow direction x, the velocity components are not the same any more for the (x, y) and the (ξ, η) reference and the tensor $\mathbf{C}_D$ is affected by the rotation of the city pattern by an angle β and now reads:

$$\mathbf{C}_D = \begin{pmatrix} C'_{\xi\xi} & C'_{\xi\eta} \\ C'_{\eta\xi} & C'_{\eta\eta} \end{pmatrix} = \mathbf{A}^{\mathrm{T}} \begin{pmatrix} C'_\xi & 0 \\ 0 & C'_\eta \end{pmatrix} \mathbf{A} \tag{6}$$

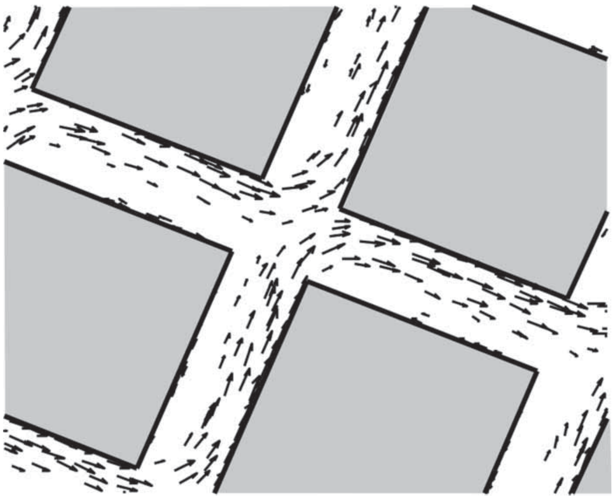

Figure 14 Computed velocity field (2D detailed model), showing that when the main flow direction is not aligned with the streets, the flow is divided and diverted at each crossroad causing additional head losses

where **A** is the rotation matrix for an angle of deviation β (for instance $\beta = -22.5°$ in the case of Fig. 3e):

$$\mathbf{A} = \begin{pmatrix} \cos\beta & \sin\beta \\ -\sin\beta & \cos\beta \end{pmatrix} \tag{7}$$

Another resistance effect occurs when the bulk velocity is not oriented along one of the principal directions ($\theta \neq 0$), which is the case for the rotated layouts, when the streets resistance are not the same in both directions. In this case, the flow is diverted and divided at each crossroad (Fig. 14) inducing additional head losses that have to be taken into account by increasing the resistance term (Velickovic, Soares-Frazão, & Zech, 2011).

If the streets have equal widths, it may be assumed that this additional head loss is the highest when the bulk velocity presents an angle of 45° with the streets and is null when the velocity is aligned with the street grid. So the drag coefficient has to be multiplied by an empirical coefficient $a > 1$ that could be defined as:

$$a = 1 + \alpha\,|\sin(2\theta)| \tag{8}$$

where α is a parameter that has to be calibrated and θ is the angle between the bulk velocity **V** and the street direction ξ as depicted in Fig. 12. Eq. (8) was designed to express the fact that the drag effect is increased when the streets are not aligned with the flow direction, the maximum increase occurring for an angle of 45° that corresponds to the larger frontal area of the obstructions when the buildings have a square shape as it is the case here. If the streets are of different widths, the maximum head loss might occur for an angle slightly different than 45° and the expression for coefficient a could also account for the ratio of street widths. However, in the present case we use Eq. (8) as such. Further work would be required to investigate the street ratio effect.

Based on these considerations, the general expression of the resistance term that has to be included in Eq. (2) reads:

$$\mathbf{S}_l = \begin{pmatrix} S_{lx} \\ S_{ly} \end{pmatrix} = a\,\frac{||\mathbf{V}||}{2g}\,(\mathbf{C}_D \cdot \mathbf{V}) \tag{9}$$

The drag tensor $\mathbf{C}_D$ represents the resistance linked to the width of the streets (conveying the fact that the resistance is higher if the streets are narrower, as it has been highlighted in the experiments of Section 2) and a expresses the increase of head loss occurring when the main flow is not aligned with the main streets as defined in Eq. (8).

3.2 *Numerical resolution and discretization*

In the present study, a finite-volume discretization is used to solve the governing equations on unstructured meshes. The fluxes are calculated by a HLL-type solver with a lateralized discretization for the pressure source term in the momentum equations (Guinot & Soares-Frazão, 2006).

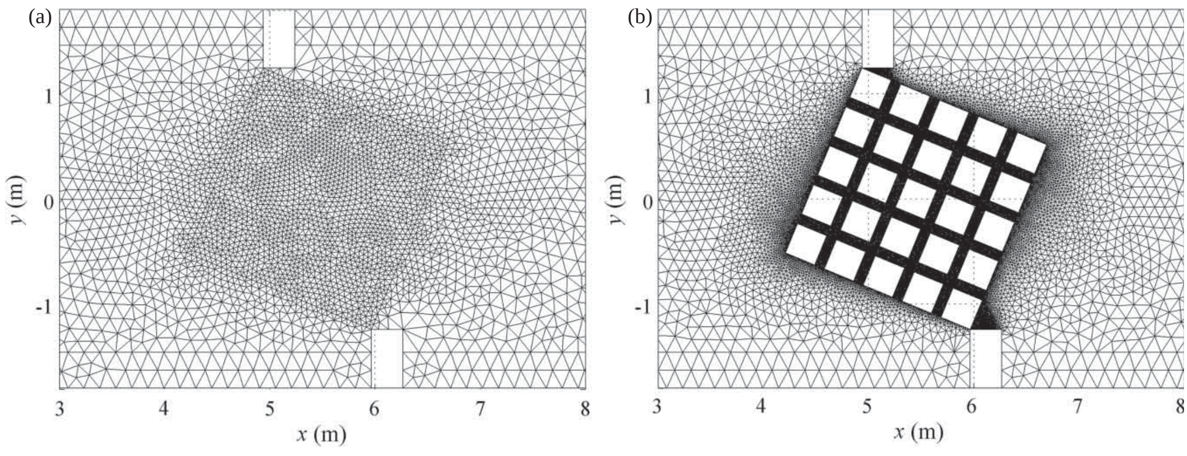

Figure 15 Computational meshes for layout A rotated: (a) porosity model with 10160 elements; (b) detailed 2D model with 46682 elements

For each experimental case, simulations are run (1) using the proposed porosity model on a coarse unstructured mesh, and (2) using a classical finite-volume resolution of the shallow-water equations on a detailed mesh including all the streets in the urban area. The coarse mesh used in the porosity model has about four times less triangular elements than the refined mesh used for the detailed approach. Figure 15 shows the computational meshes used for layout A rotated (Fig. 3b) around the urban area: the coarse mesh has 10,160 elements while the detailed mesh has 46,682 elements. All simulations were run with a CFL number of 0.9.

4 Calibration of the drag parameters

The objective of this section is to show how the experimental data described in Section 2 can be used to calibrate and validate the porosity model, with a focus on the validation of the drag resistance expression of Eq. (9). Indeed, the drag resistance is more important than the friction effects in a configuration like the one considered here.

In a first step, the drag tensors will be calibrated for steady flows through the aligned layouts A (Fig. 3a), B with wide streets in the x-direction (Fig. 3c) and B with narrow streets in the x-direction (Fig. 3d). As the flow is oriented in the direction of the streets, the coefficient a (Eq. 8) is equal to one and has no influence on the computed flow. Also, as the principal directions (ξ, η) are aligned with the axes of coordinates (x, y), the non-diagonal component of the drag tensor will be equal to zero (Bear, 1972). In the following sections, the procedure to calibrate the drag parameters is described first for the isotropic cases where all the streets have an equal width in the ξ- and η-directions, then for the anisotropic cases and finally the rotation of the urban area is considered.

4.1 *Isotropic cases*

The drag tensor in the case of the regular layout A of Fig. 3a, where the main flow direction is aligned with the streets, is:

$$\mathbf{C}_D^{(a)} = \begin{pmatrix} C'_\xi & 0 \\ 0 & C'_\eta \end{pmatrix} = \begin{pmatrix} C_D^{\mathrm{iso}} & 0 \\ 0 & C_D^{\mathrm{iso}} \end{pmatrix} = C_D^{\mathrm{iso}} \mathbf{I} \tag{10}$$

where $\mathbf{I}$ is the identity matrix, and the superscript (a) denotes the layout of Fig. 3a. Notice that, as this layout is regular, the drag tensor does not depend on its orientation (Bear, 1972) and takes a diagonal form similar to an isotropic case, regardless of the orientation of the urban area. This implies that the tensor of the regular rotated layout (b) of Fig. 3 is the same, i.e. $\mathbf{C}_D^{(b)} = \mathbf{C}_D^{(a)}$. Indeed, as $\mathbf{C}_D^{(a)} = \mathbf{C}_D^{\mathrm{iso}}\mathbf{I}$, the rotation does not affect the matrix. So only the coefficient C_D^{iso} has to be calibrated. It must however be noted that for the rotated case, an additional parameter a is involved in the drag Eq. (9). This parameter is discussed further.

4.2 *Anisotropic cases*

For the anisotropic layout (defined here as the case where the streets have different widths in the two principal directions), two drag coefficients have to be calibrated, one for each principal direction. The drag coefficient associated to the narrow streets will be calibrated with the layout (c) of Fig. 3c, with the narrow streets in the x-direction, which is also the ξ-direction. Indeed, the drag tensor for this layout is:

$$\mathbf{C}_D^{(c)} = \begin{pmatrix} C'_\xi & 0 \\ 0 & C'_\eta \end{pmatrix} = \begin{pmatrix} C_D^{\mathrm{narrow}} & 0 \\ 0 & C_D^{\mathrm{wide}} \end{pmatrix} \tag{11}$$

As the bulk velocity through the urban area will be principally directed in the x-direction, $v \cong 0$ and the computed flow will be practically insensitive to the value of C_D^{wide}, allowing C_D^{narrow} to be calibrated independently.

The coefficient C_D^{wide} will then be calibrated with the layout of Fig. 3d with the wide streets in the x-direction, independently from C_D^{narrow}. The drag tensor in this case reads:

$$\mathbf{C}_D^{(d)} = \begin{pmatrix} C'_\xi & 0 \\ 0 & C'_\eta \end{pmatrix} = \begin{pmatrix} C_D^{\mathrm{wide}} & 0 \\ 0 & C_D^{\mathrm{narrow}} \end{pmatrix} \tag{12}$$

4.3 *Rotated cases*

When the urban area presents a deviation of angle β as defined e.g. in Fig. 3e, the corresponding drag tensor for this medium is obtained from the drag tensor of the aligned case multiplied by a rotation matrix $\mathbf{A}$:

$$\mathbf{C}_D = \mathbf{A}^{\mathrm{T}} \begin{pmatrix} C'_\xi & 0 \\ 0 & C'_\eta \end{pmatrix} \mathbf{A} \tag{13}$$

where $\mathbf{A}$ is the rotation matrix for an angle of deviation β. ($\beta = -22.5°$ in the case of Fig. 3e):

$$\mathbf{A} = \begin{pmatrix} \cos\beta & \sin\beta \\ -\sin\beta & \cos\beta \end{pmatrix} \tag{14}$$

Then, for the rotated cases, the parameter α in Eq. (8) is calibrated using the rotated regular layout (b) of Fig. 3b, for which the drag tensor is identical to the drag tensor of the aligned regular case.

4.4 *Result of the calibration procedure*

The above described procedure has been used for the different experimental layouts: the drag coefficients were calibrated from the three aligned layouts, while the parameter α of the amplification factor a was deduced from the rotated experiments, assuming that the drag coefficients have not been modified.

For each tested case, the quality of the calibration was assessed by comparing the measured and computed water level upstream of the urban area over the whole range where experimental data are available. Indeed, this level is considered as being representative of the effect of the flow resistance induced by the presence of the urban area. The relative error is characterized by the coefficient of variation of the normalized root-mean-square deviation:

$$\mathrm{CV(RMSD)} = \frac{1}{\bar{h}_{exp}}\sqrt{\frac{\sum (h_{exp} - h_{num})^2}{n}} \tag{15}$$

Table 2 gives the results of this calibration, each typical layout being used for a specific parameter. For each layout, the coefficient of variation of RSMD obtained for the different tested discharges is indicated. The low error values indicate that the calibrated parameters are valid over the whole range of considered discharges.

The results of the porosity model are also compared to the detailed 2D approach (Soares-Frazão & Zech, 2008) and to the experimental observations over the whole flow range, as illustrated in the following figures.

The results of the simplest case (case A aligned, layout of Fig. 3a, results in Fig. 16) highlight the differences between the modelling approaches for the head losses through the urban area. The experiments show that most of the head loss occurs at the entrance and the exit of the city, which is logical due to expansion of the flow. The detailed 2D model appears to overestimate the exit effect. The porosity model represents well the whole head loss, but this head loss is fictitiously distributed along the whole length and not concentrated at the

Table 2 Parameter calibration for the layouts of Fig. 3 (steady flow)

Layout	Ref. to Fig. 3	Q (l s^{-1})	Parameter calibrated	CV(RMSD) (%)
A aligned	3a	43, 58, 63, 75, 86, 103	$C_D^{\mathrm{iso}} = 4.5$	2.36
B aligned narrow	3c	25; 35; 41; 50	$C_D^{\mathrm{narrow}} = 15.0$	0.91
B aligned wide	3d	52; 64; 75; 80; 92; 99	$C_D^{\mathrm{wide}} = 2.0$	1.19
A rotated	3b	75; 100	$\alpha = 5$	1.25

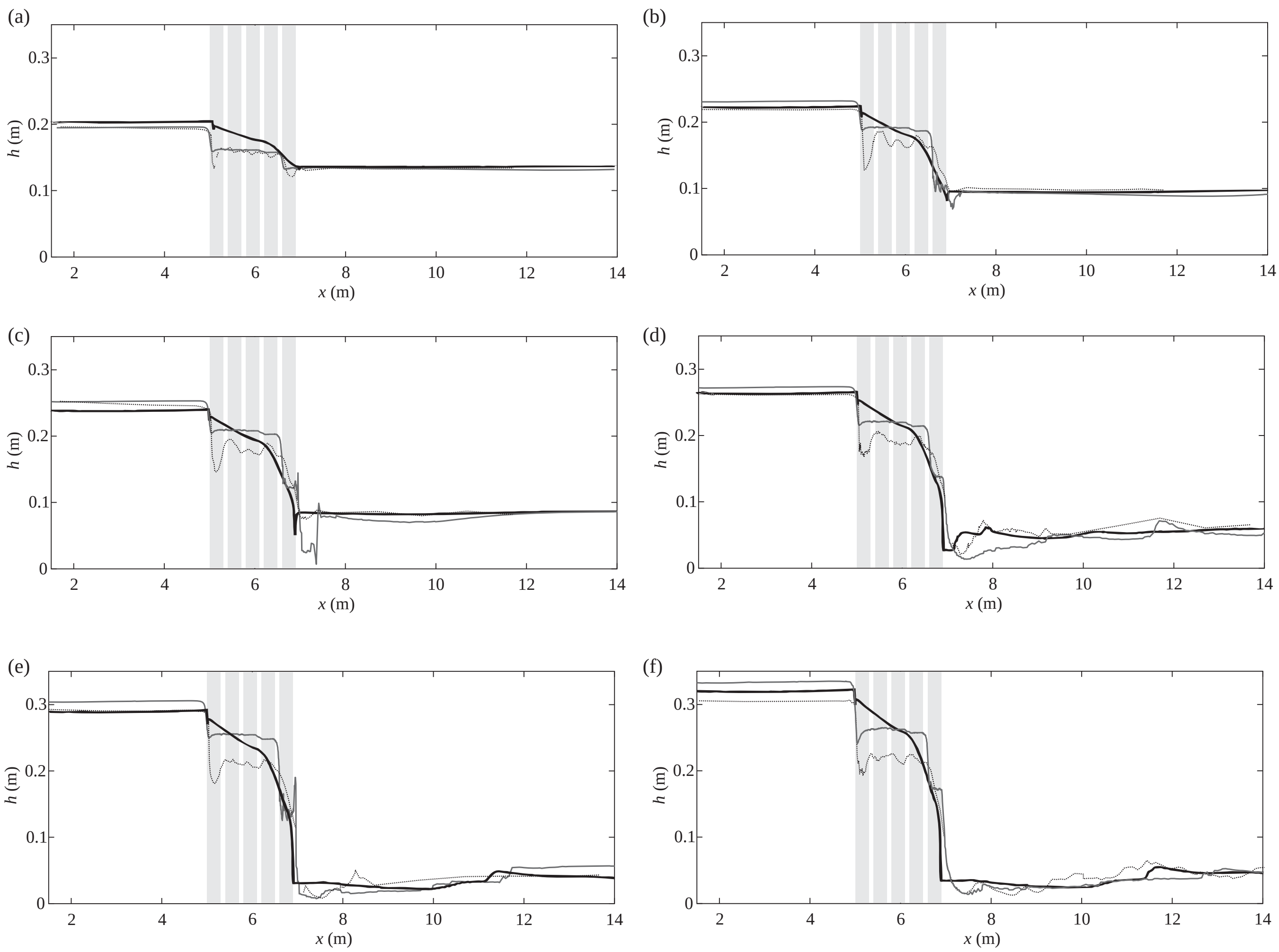

Figure 16 Case A aligned (Fig. 3a). Results along axis 1, with $C'_\xi = 4.5$, for the experiments (dotted line), the porosity model (thick black line), the 2D detailed model (grey line): (a) $Q = 43\,\mathrm{l\,s^{-1}}$; (b) $Q = 58\,\mathrm{l\,s^{-1}}$; (c) $Q = 63\,\mathrm{l\,s^{-1}}$; (d) $Q = 75\,\mathrm{l\,s^{-1}}$; (e) $Q = 86\,\mathrm{l\,s^{-1}}$; (f) $Q = 103\,\mathrm{l\,s^{-1}}$

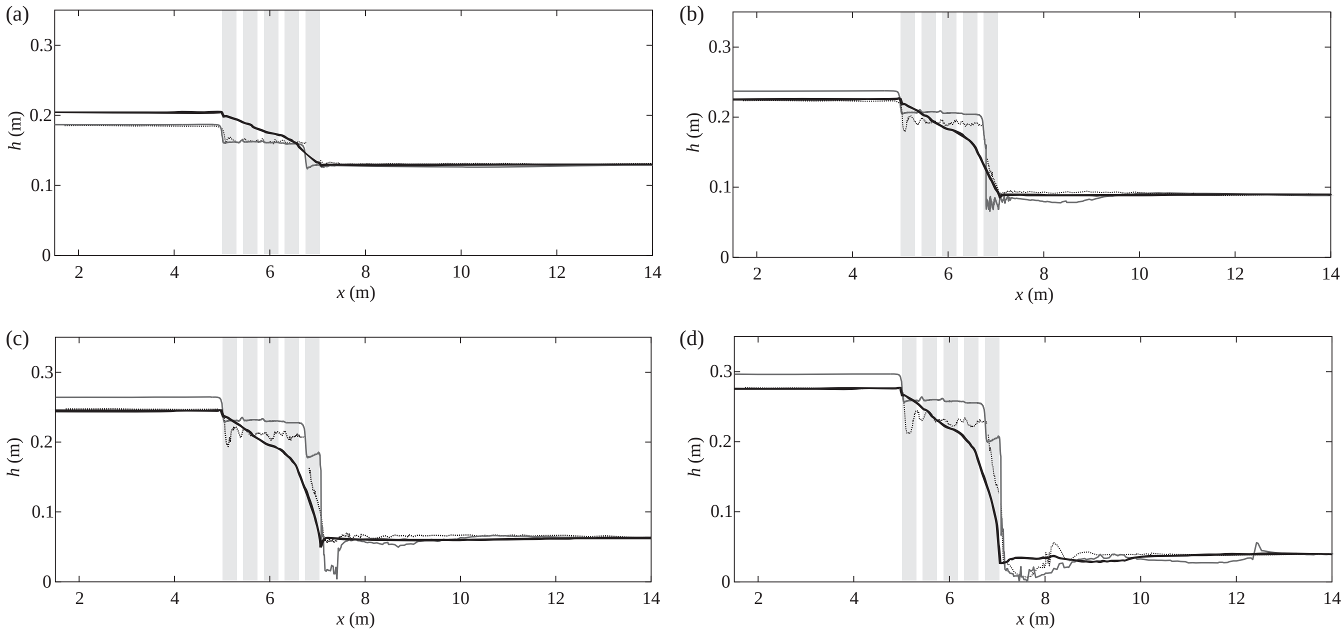

Figure 17 Case B aligned narrow (Fig. 3c). Results along axis 1, with $C'_\xi = 15.0$, for the experiments (dotted line), the porosity model (thick black line), the 2D detailed model (grey line): (a) $Q = 25\,\mathrm{l\,s^{-1}}$; (b) $Q = 35\,\mathrm{l\,s^{-1}}$; (c) $Q = 41\,\mathrm{l\,s^{-1}}$; (d) $Q = 50\,\mathrm{l\,s^{-1}}$

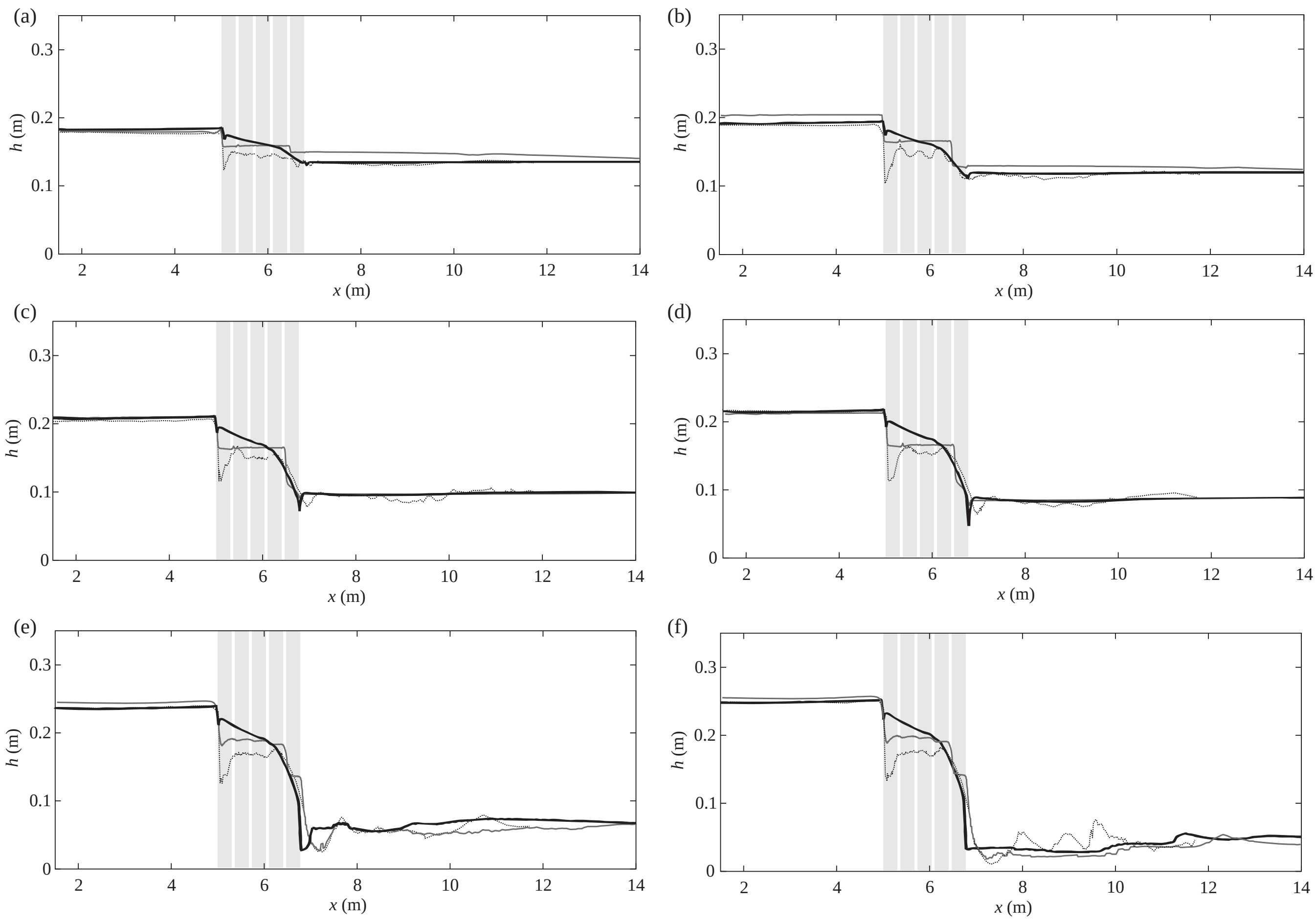

Figure 18 Case B aligned wide (Fig. 3d). Results along axis 1, with $C'_\xi = 2.0$, for the experiments (dotted line), the porosity model (thick black line), the 2D detailed model (grey): (a) $Q = 52\,\mathrm{l\,s^{-1}}$; (b) $Q = 64\,\mathrm{l\,s^{-1}}$; (c) $Q = 75\,\mathrm{l\,s^{-1}}$; (d) $Q = 80\,\mathrm{l\,s^{-1}}$; (e) $Q = 92\,\mathrm{l\,s^{-1}}$; (f) $Q = 99\,\mathrm{l\,s^{-1}}$

entrance and the exit, which is logical for this continuum approach.

The results of the anisotropic cases (case B narrow aligned, layout of Fig. 3c, results in Fig. 17 and case B wide aligned, layout of Fig. 3d, results in Fig. 18) are comparable to the results of the regular (isotropic) aligned case. The calibrated drag coefficient for the narrow and the wide streets, respectively, lead to excellent results regarding the total head loss, except for the smallest discharge ($25\,\mathrm{l\,s^{-1}}$) in the case B narrow, Fig. 17): for this discharge it was observed that the flow along the narrow streets was strongly controlled by viscosity, so poorly described by a model assuming a full turbulence regime. In addition, it is interesting to observe that the detailed 2D approach tends to overestimate the head losses through the urban area.

The results of the rotated case (case A rotated, layout of Fig. 3b, results in Fig. 19) are really satisfactory: the porosity model captures the total head loss, even better than the detailed 2D model.

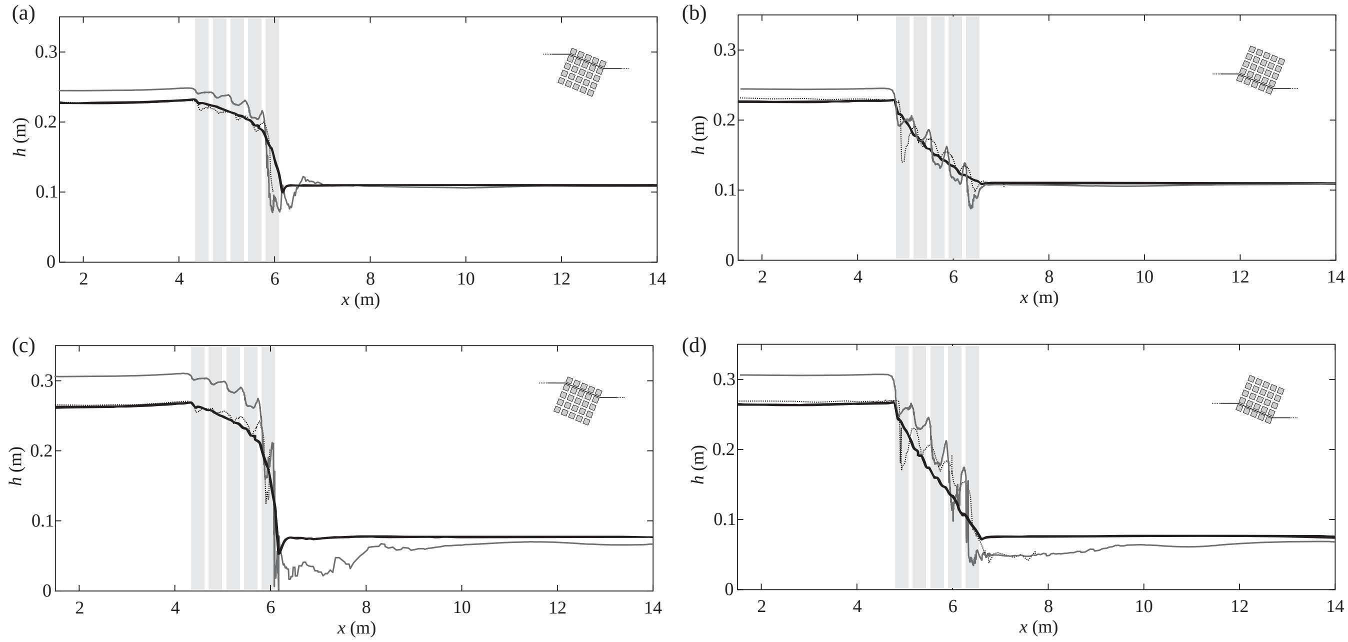

Figure 19 Case A aligned rotated (Fig. 3b). Results with $C'_{\xi} = 4.5.0$, for the experiments (dotted line), the porosity model (thick black line), the 2D detailed model (grey): (a) along axis 1, $Q = 75\,\mathrm{l\,s^{-1}}$; (b) along axis 4, $Q = 75\,\mathrm{l\,s^{-1}}$; (c) along axis 1, $Q = 100\,\mathrm{l\,s^{-1}}$; (d) along axis 4, $Q = 100\,\mathrm{l\,s^{-1}}$

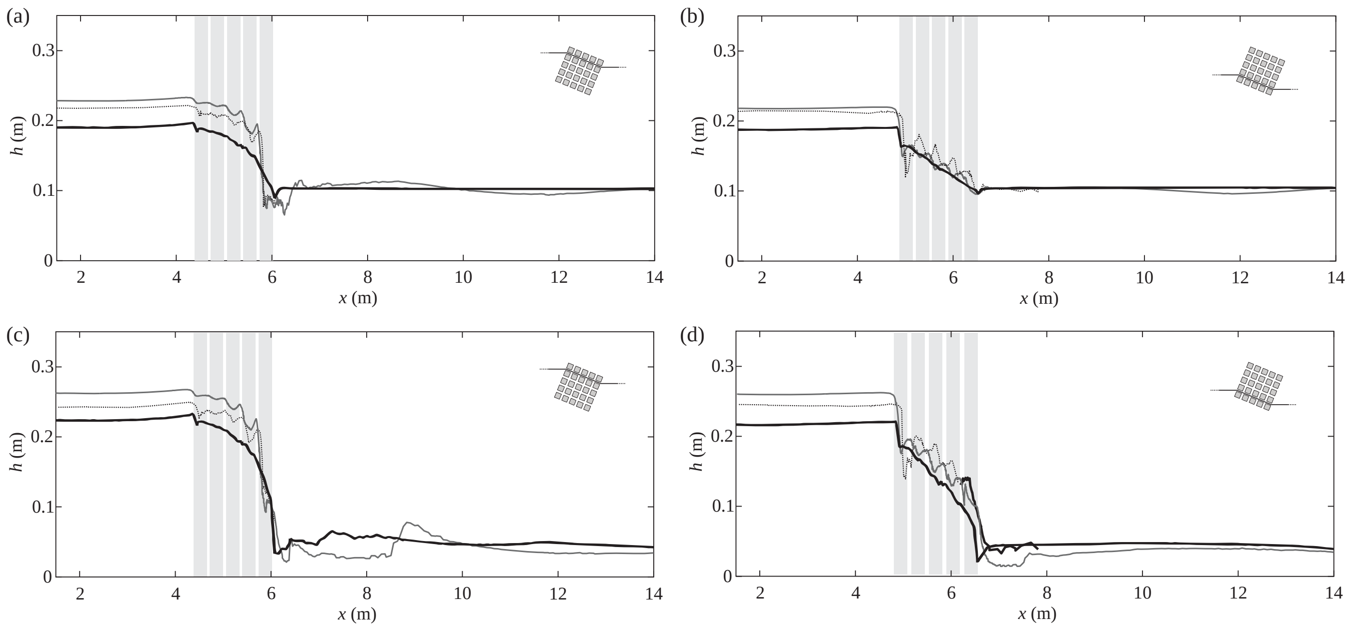

Figure 20 Case B rotated (Fig. 3e). Results with $\mathbf{C}_D$ as defined in (16), for the experiments (dotted line), the porosity model (thick black line), the 2D detailed model (grey): (a) along axis 1, $Q = 75\,\mathrm{l\,s^{-1}}$; (b) along axis 4, $Q = 75\,\mathrm{l\,s^{-1}}$; (c) along axis 1, $Q = 100\,\mathrm{l\,s^{-1}}$; (d) along axis 4, $Q = 100\,\mathrm{l\,s^{-1}}$

5 Validation of the proposed model and parameters

The rotated anisotropic case (case B rotated, Fig. 3e) is used to validate the whole procedure. The drag tensor is obtained as follows:

$$\mathbf{C}_D^{(e)} = \mathbf{A}^{\mathrm{T}} \begin{pmatrix} C_{wide} & 0 \\ 0 & C_{narrow} \end{pmatrix} \mathbf{A} = \begin{pmatrix} 3.9 & 4.6 \\ 4.6 & 13.1 \end{pmatrix} \qquad (16)$$

where $\mathbf{A}$ is the rotation matrix corresponding to an angle $\beta = -22.5°$. The amplification parameter α is kept equal to 5, and parameter a is calculated according to Eq. (8). The results obtained with the porosity model are illustrated in Fig. 20 and compared to both the measurements and to the detailed 2D model.

The results of the anisotropic rotated case (case B rotated, layout of Fig. 3e, results in Fig. 20) are less satisfactory in terms of water levels: the porosity model appears to underestimate the total flow resistance, while the 2D model rather overestimates this. So, the combination of the amplification factor a in Eq. (8) due the non-alignment with the drag tensor $\mathbf{C}_D$ in Eq. (16) due to the anisotropy is less convincing than each effect considered separately.

However, the model performs well in adapting the velocity direction to the actual layout of the medium, as illustrated in Fig. 21. The velocity field issued from the detailed 2D simulation (Fig. 21a and 21b) presents high velocities in the streets with a main orientation of the flow along the wide streets. This feature is well reproduced by the porosity model with the anisotropic drag tensor (Fig. 21c).

6 Conclusions

The concept of porosity applied to an urban area allows for a bulk representation of the flow through this area, including the

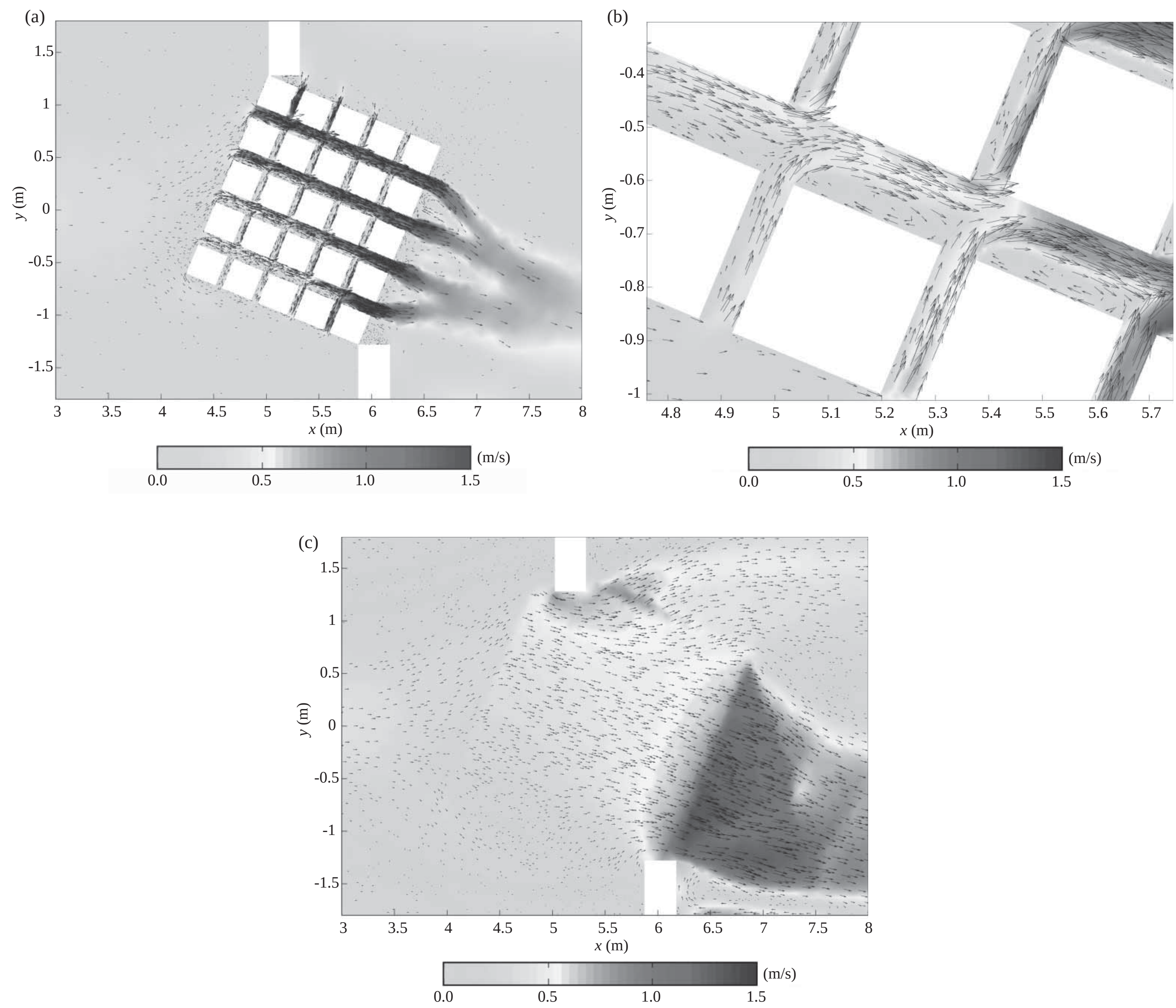

Figure 21 Comparison of velocity fields computed with (a, b) the detailed 2D model and (c) the porosity model

increased flow resistance offered by the buildings. The effects of the arrangement of the streets and buildings were studied using both laboratory experiments and numerical modelling.

A series of idealized urban areas configurations have been tested in steady flow conditions, each of these configurations featuring an ensemble of 5 × 5 blocks, with wider and narrower streets, aligned or not with the main flow direction. These different arrangements formed urban areas that could be considered as isotropic or anisotropic porous media. A significant decrease of the water depth at the entrance and at the exit of the urban area was observed, with, in some cases, depending on the total discharge, a control section and a jump at the exit. The influence of the city layout, isotropic or anisotropic, aligned or rotated compared to the main flow direction, could be clearly highlighted. In particular, it was observed that an isotropic configuration not aligned with the main flow direction resulted in a higher flow resistance than the same configuration where the streets were aligned with the main flow direction.

A porosity model is proposed for the representation of these resistance effects on the flow, accounting for the non-alignment of the main streets to the main flow direction and for the deviation of the bulk velocity to the direction of the streets. A tensor of drag coefficients according to the flow direction is used with an amplification factor for deviated celerities. Based on the experimental data, a strategy is proposed for the calibration of the drag coefficients and the amplification factor. This strategy consists in calibrating each parameter separately using basic configurations where this parameter controls the dominant effects.

For those various configurations, the results obtained using the porosity model were compared to a detailed 2D model with accurate representation of the streets and to the experimental measurements. The porosity model proved to be accurate regarding the prediction of the total depth drop through the city, except in the case where the urban area was both rotated and anisotropic. However, improvements are still required to propose a model combining satisfactorily the effects. As regards the velocity field, the anisotropic porosity model was able to reproduce the change in flow direction imposed by the presence of an urban area with preferential flow directions.

Future work will be devoted to other configurations, for example with a varying number of blocks in order to improve and generalize the methodology and to fix a general calibration procedure for the different parameters of the model.

Funding

The first author was funded by the Fonds pour la Formation à la Recherche dans l'Industrie et dans l'Agriculture (FRIA), Belgium.

Notation

a = drag amplification factor (–)
g = gravity acceleration (m s^{-2})
h = water depth (m)
Q = discharge (usually m^{3}s^{-1}, but often l s^{-1} for clarity in the text)
S_0 = bed slope (–)
S_f = friction head loss slope
S_l = part of head-loss slope due to drag forces losses (–)
t = time (s)
u = longitudinal depth-averaged bulk velocity, i.e. in the x-direction (m s^{-1})
v = transversal depth-averaged bulk velocity, i.e. in the y-direction (m s^{-1})
x = coordinate in the longitudinal direction (m)
y = coordinate in the transversal direction (m)
$\mathbf{A}$ = rotation matrix
$\mathbf{C}_D$ = drag tensor
$\mathbf{F}$ = vector of fluxes in the x-direction
$\mathbf{G}$ = vector of fluxes in the y-direction
$\mathbf{I}$ = identity matrix
$\mathbf{n}$ = unit vector indicating the normal direction
$\mathbf{V}$ = bulk velocity vector
$\mathbf{S}$ = vector of source terms
α = calibration parameter (–)
β = angle of inclination of the city streets with respect to the main flow direction
ϕ = porosity (–)

ORCID

Sandra Soares-Frazão http://orcid.org/0000-0001-5088-0278

References

Araud, Q., Finaud-Guyot, P., Lawniczak, F., Francois, P., Mose, R., & Vazquez, J. (2012). *Modeling flood in an urban area: Validation of numerical tools against experimental data*. Simhydro, September 12–14 2012, Nice, France.

Bachmat, Y., & Bear, J. (1986). Macroscopic modelling of transport phenomena in porous media. 1: The continuum approach. *Transport in Porous Media*, *1*, 213–240.

Bates, P. D. (2000). Development and testing of a subgrid-scale model for moving-boundary hydrodynamic problems in shallow water. *Hydrological Processes*, *14*(11–12), 2073–2088.

Bazin, P. H. (2013). *Flows during floods in urban areas: Influence of the detailed topography and the exchanges with the sewer system* (PhD dissertation). Université Claude Bernard, Lyon. Retrieved from https://hal.inria.fr/tel-01159518/document

Bear, J. (1972). *Dynamics of fluids in Porous materials*. New-York: Elsevier (reprinted by Dover Publications, 1988).

Cea, L., & Vázquez-Cendón, M. E. (2010). Unstructured finite volume discretization of two-dimensional depth-averaged shallow water equations with porosity. *International Journal for Numerical Methods in Fluids*, *63*, 903–930.

Defina, A. (2000). Two-dimensional shallow flow equations for partially dry areas. *Water Resources Research*, *36*, 3251–3264.

Defina, A., D'Alpaos, L., & Mattichio, B. (1994). A new set of equations for very shallow water and partially dry areas suitable to 2D numerical models. In P. Molinaro & L. Natale (Eds.), *Proceedings of the specialty conference on modelling of flood propagation over initially dry areas* (pp. 72–81). New York: American Society of Civil Engineers.

Finaud-Guyot, P., Delenne, C., Lhomme, J., Guinot, V., & Llovel, C. (2010). An approximate-state Riemann solver for the two-dimensional shallow water equations with porosity. *International Journal for Numerical Methods in Fluids*, *62*, 1299–1331.

Gallegos, H. A., Schubert, J. E., & Sanders, B. F. (2009). Two-dimensional, high-resolution modeling of urban dam-break flooding: A case study of Baldwin Hills, California. *Advances in Water Resources*, *32*, 1323–1335.

Guinot, V. (2012). Multiple porosity shallow water models for macroscopic modelling of urban floods. *Advances in Water Resources*, *37*, 40–72.

Guinot, V., & Soares-Frazão, S. (2006). Flux and source term discretization in two-dimensional shallow water models with porosity on unstructured grids. *International Journal for Numerical Methods in Fluids*, *50*, 309–345.

Ishigaki, T., Keiichi, T., & Kazuya, I. (2003). *Hydraulic model tests of inundation in urban area with underground space*. XXX IAHR Congress, Thessaloniki, Greece.

Ishigaki, T., Nakagawa, H., & Baba, Y. (2004). Hydraulic model test and calculation of flood in urban area with underground space. In J.H.W. Lee & K.M. Lam (Eds.), *Environmental hydraulics and sustainable water management* (Vol. 1, pp. 1411–1416). Boca Raton, FL: Taylor & Francis.

Kim, B. H., Sanders, B. F., Famiglietti, J. S., & Guinot, V. (2015). Urban flood modeling with porous shallow-water equations: A case study of model errors in the presence of anisotropic porosity. *Journal of Hydrology*, *523*, 680–692.

Lhomme, J. (2006). *Modélisation des inondations en milieu urbain: approches unidimensionnelle, bidimensionnelle et macroscopique* (PhD thesis). Université Montpellier 2, Montpellier [in French].

Lhomme, J., Soares-Frazão, S., Guinot, V., & Zech, Y. (2007). Modélisation à grande échelle des inondations urbaines et modèle 2D à porosité. *La Houille Blanche*, *4*, 104–110.

Liang, D., Falconer, R. A., & Lin, B. (2007). Coupling surface and subsurface flows in a depth averaged flood wave model. *Journal of Hydrology*, *337*, 147–158.

Mason, D. C., Horritt, M. S., Hunter, N. M., & Bates, P. D. (2007). Use of fused airborne scanning laser altimetry and digital map data for urban flood modelling. *Hydrological Processes*, *21*, 1436–1447.

McMillan, H. K., & Brasington, J. (2007). Reduced complexity strategies for modelling urban floodplain inundation. *Geomorphology*, *90*, 226–243.

Paquier, A., Tachrift, H., Riviere, N., & El Kadi, K. (2009, November 26–27). Assessing the effects of two non-structural flood mitigation measures using laboratory and real cases. Road map towards a flood resilient urban environment. *Proceedings final conference of the COST action C22*, Paris, France. 8p.

Sanders, B. F., Schubert, J. E., & Gallegos, H. A. (2008). Integral formulation of shallow-water equations with anisotropic porosity for urban flood modeling. *Journal of Hydrology*, *362*, 19–38.

Schubert, J. E., Sanders, B. F., Smith, M. J., & Wright, N. G. (2008). Unstructured mesh generation and landcover-based resistance for hydrodynamic modeling of urban flooding. *Advances in Water Resources*, *31*, 1603–1621.

Soares-Frazão, S., Lhomme, J., Guinot, V., & Zech, Y. (2008). Two-dimensional shallow-water model with porosity for urban flood modelling. *Journal of Hydraulic Research*, *46*(1), 45–64.

Soares-Frazão, S., Spinewine, B., Duthoit, A., Deswijsen, J. F., & Zech Y. (2006). Dam-break flow experiments in simplified city layouts. In *Proceedings river flow 2006 international conference on fluvial hydraulics* (pp. 513–521), Lisbon, Portugal.

Soares-Frazão, S., & Zech, Y. (2008). Dam-break flow through an idealised city. *Journal of Hydraulic Research*, *46*(5), 648–658.

Testa, G., Zuccalà, D., Alcrudo, F., Mulet, J., & Soares-Frazão, S. (2007). Flash-flood flow experiment in a simplified urban district. *Journal of Hydraulic Research*, *45*(Extra issue), 37–44.

Velickovic, M. (2012). *Macroscopic modeling of urban flood with a porosity model* (PhD thesis). Université catholique de Louvain, Louvain-la-Neuve.

Velickovic, M., Soares-Frazão, S., & Zech, Y. (2011). Porosity model of flow through an idealised urban district: Influence of city alignment and of transient flow character. *Proceedings 34th world congress international association of hydraulic engineering and research* (pp. 3823–3830), Brisbane, Australia.

Velickovic, M., Van Emelen, S., Zech, Y., & Soares-Frazão (2010). Shallow-water model with porosity: Sensitivity analysis to head losses and porosity distribution. *Proceedings River Flow 2010 conference* (Vol. 1, pp. 613–620), Braunschweig, Germany.

Velickovic, M., Zech, Y., & Soares-Frazão, S. (2012). Modeling of flood in urban areas with a porosity model: Directional effects. *Proceedings River Flow 2012 conference* (Vol. 1, pp. 347–353), San Jose, Costa Rica. Retrieved from http://hdl.handle.net/2078/118599